Xu, Donghan; Zhang, Cuijuan; Zhen, Yihan; Zhao, Yicheng; Li, Yongdan

A high-rate nonaqueous organic redox flow battery

Published in:
Journal of Power Sources

DOI:
10.1016/j.jpowsour.2021.229819

Published: 31/05/2021

Document Version
Peer-reviewed accepted author manuscript, also known as Final accepted manuscript or Post-print

Please cite the original version:
Xu, D., Zhang, C., Zhen, Y., Zhao, Y., & Li, Y. (2021). A high-rate nonaqueous organic redox flow battery. *Journal of Power Sources*, *495*, Article 229819. https://doi.org/10.1016/j.jpowsour.2021.229819

A High-Rate Nonaqueous Organic Redox Flow Battery

Donghan Xu[a,b], Cuijuan Zhang[a,b,*], Yihan Zhen[a,b], Yicheng Zhao[a,b], Yongdan Li[a,b,c,*] *

[a] State Key Laboratory of Chemical Engineering, Tianjin Key Laboratory of Applied Catalysis Science and Technology, School of Chemical Engineering and Technology, Tianjin University, Tianjin 300072, China. Email: cjzhang@tju.edu.cn

[b] Collaborative Innovation Center of Chemical Science and Engineering (Tianjin), Tianjin 300072, China

[c] Department of Chemical and Metallurgical Engineering, School of Chemical Engineering, Aalto University, Kemistintie 1, Espoo, P.O. Box 16100, FI-00076, Aalto, Finland. Email: yongdan.li@aalto.fi

Abstract: Azobenzene (azoB) is a promising anode active material for nonaqueous redox flow battery (NARFB), but the battery performance assembled with azoB is rather poor. Here, we show that the rate performance of NARFB with azoB and 2,5-di-tert-butyl-1-methoxy-4-[2'-methoxyethoxy] benzene (DBMMB) as anolyte and catholyte active materials can be significantly enhanced by optimizing the solvent, supporting electrolyte, and membrane. The synergistic interaction among active materials, solvent (acetonitrile), supporting electrolyte (tetraethylammonium bis(trifluoromethylsulfonyl)imide), and membrane (Daramic 175) contributes to the high battery performance. It exhibits an energy efficiency of 63.5% even at an ultra-high current density of 100 mA cm^{-2}. Furthermore, the battery delivers a peak power density of 336 mW cm^{-2} at the current density of 240 mA cm^{-2} with 0.25 M active materials, which is a new benchmark for NARFBs.

Keywords: Electrochemical energy storage, nonaqueous redox flow battery, organic electroactive material

1. Introduction

Redox flow batteries (RFBs) characterized by decoupling of energy and power outputs have been receiving increasing interest for the large-scale energy storage [1, 2]. Conventional aqueous RFBs are limited by the narrow operating voltage window (~ 1.6 V) due to the water electrolysis and thus low energy densities (< 25 Wh L^{-1}) [3, 4]. In contrast, the nonaqueous RFBs (NARFBs) provide an alternative to achieve high energy densities due to the wider electrochemical windows (e.g., > 2 V) of the active materials and solvents [5]. A variety of materials can be used as active species for NARFBs such as redox active polymers [6], organometallic compounds [7] and redox-active organic materials (ROMs) [8-11]. Among them, ROMs including metallocene, carbonyl, nitroxide radical, alkoxybenzene and heteroaromatics stand out because of their structural diversity, adjustable solubility, environmental friendliness and potentially low price [1, 5], which make it feasible to construct a flow battery with high open circuit voltage, improved energy density and low price.

The recent years have witnessed the rapid progress of NARFBs. Nevertheless, many challenges need to be addressed before possible application. One is the high capital cost mainly due to large stack areas for the specific energy to power ratio (E/P) [12]. An effective solution is to maximize the power density and maintain high energy efficiency (EE), which makes it possible to use smaller sized battery stack and to obtain higher electrolyte utilization rate. To achieve high power density, both high battery voltage and large current density (j) are needed. As the operating j increases, i.e., higher rate-capability, the voltage losses (activation loss, ohmic loss and concentration loss) become worse, which reduces the electrolyte utilization and also voltage efficiency (VE) [13, 14]. Accordingly, the current NARFBs generally operate at relatively low j, rarely exceeding 40 mA cm^{-2}

[15-17].

The voltage and rate capability of NARFBs are closely dependent on the active materials, supporting electrolyte, solvent, and the membrane. Firstly, as the core components, the active materials fundamentally determine the open circuit voltage (OCV) and the electrode kinetics of the flow battery. A large potential difference between cathode and anode redox couples contributes to a high OCV. Furthermore, a rapid kinetics at the electrodes is of importance to achieve excellent performance at high current densities. Various active materials have been reported. Huo et al. [18] achieved a significantly high OCV of 2.97 V based on 4,4′-dimethylbenzophenone (44DMBP) anolyte and 2,5-di-tert-butyl-1,4-dimethoxybenzene (DBB) catholyte. However, the resultant battery showed low EE of only ~30% at 1 mA cm^{-2}. Duan et al. [10] developed a NARFB with 2,1,3-benzothiadiazole (BzNSN)/2,5-di-tert-butyl-1-methoxy-4-[2'-methoxyethoxy]benzene (DBMMB) active materials, and proposed that the large electrochemical rate constants (0.9×10^{-2} cm s^{-1} for BzNSN reduction and 1.0×10^{-2} cm s^{-1} for DBMMB oxidation) contribute to EE of ~70% at 40 mA cm^{-2}. Very recently, Zhang et al. [19] reported a NARFB based on azobenzene (azoB) and DBMMB in lithium bis(trifluoromethanesulfonyl)imide (LiTFSI)/dimethylformamide (DMF) with an OCV of ~2.5 V, which achieved a peak power density of 170 mW cm^{-2}. However, such battery showed short cycling life with serious capacity degradation.

The supporting electrolyte and solvent determine the electrolyte conductivity. Tetraethylammonium (TEA^{+})-based salts are widely used in NARFBs as support electrolyte [5]. It has been reported that the electrolytes containing acetonitrile (MeCN) and (TEA^{+})-based salts have considerably higher conductivities than most other electrolytes [8]. In addition, the electron spin resonance (ESR) results revealed that the bulky cation TEA^+ in tetraethylammonium bis(trifluoromethylsulfonyl)imide (TEATFSI) has less harmful effect on the stability of radicals than LiTFSI [8].

The membrane also affects the performance of NARFBs, since it not only transfers the supporting electrolyte, but also prevents crossover of the active materials. Compared to the organic and ceramic membranes, the porous separators show lower area-specific resistance (ASR), which contributes to reduced battery internal resistance and thus to higher power density [20]. Wei et al. evaluated several commercial porous separators with different thicknesses and porosity and found that Daramic 175 separator demonstrates fairly low ASR ($< 3\ \Omega\ cm^2$) [9], and is suitable for high current density battery. However, due to the relatively large pore size, a mixed-reactant electrolyte design is always used to reduce the concentration gradient and alleviate the crossover of the redox-active materials [9].

Herein, to maximize the performance of the battery with azoB and DBMMB as active materials, we optimize the supporting electrolyte, solvent and separator. The results show that the optimized cell achieved an EE of 63.5% even at j of as high as 100 mA cm^{-2}. Furthermore, the azoB/DBMMB cell delivered a peak power density of 336 mW cm^{-2}, representing the highest peak power density for NARFBs in the open literature to the best of our knowledge.

2. Experimental

2.1. Material

MeCN (Sigma-Aldrich, 99.9%), DMF (Aladdin, 99.9%), ethanol (Yuanli, 99.7%)) and $AgNO_3$ (Aladdin, 99.8%) were used as received. AzoB (TCL, 98%) was further purified by recrystallization from ethanol. DBMMB and TEATFSI were synthesized according to the reported procedures [21, 22].

2.2. Electrochemical test

Cyclic voltammetry (CV) data were collected on a VersaSTAT 3 electrochemical workstation (Princeton Applied Research, USA) in a standard three-electrode system with a glassy carbon working electrode (6 mm diameter), a graphite plate counter electrode (5.24 cm^2), and a Ag/Ag^+ (0.5 M $AgNO_3$/MeCN) reference electrode. The electrolyte is the mixture of azoB-DBMMB at a mole ratio of 1:1 and TEATFSI dissolved in MeCN. Before the test, the system was bubbled with argon (Liufang, 99.999%) for 10 min to remove oxygen.

Linear sweep voltammetry (LSV) tests were performed on a CHI604D electrochemical workstation (Shanghai Chenhua Instruments Co., China) at room temperature in argon with a BASI RDE-2 rotator configuration (Bioanalytical Systems, Inc., USA). The Teflon encased glassy carbon rotating disk electrode (RDE, 5 mm in diameter, AFMSRCE 061906, PINE), graphite plate (5.24 cm^2), and Ag/Ag^+ (0.5 M $AgNO_3$/MeCN) served as the working, counter, and reference electrodes, respectively. The working electrode was rotated from 100 to 600 rpm. The electrolyte of 0.01 M azoB or DBMMB in 1.0 M TEATFSI/MeCN was prepared and tested at a scan rate of 5 mV s^{-1}. The kinematic viscosity was measured as 0.0090 cm^2 s^{-1} on capillary viscometer.

The flow cells with a home-designed configuration were tested in an argon-filled glove box. The graphite felts (Morgan WDF-5) were employed as electrodes and the active size was 2 cm wide × 2 cm long. The commercial separator Daramic-175 (175 μm in thickness) was selected, which is composed of polyethylene/silica and is porous with the median pore size of 0.15 mm and porosity of

57%. The separator and graphite felt electrodes were ultrasonically cleaned with ethanol and dried under vacuum before test. The electrolytes (10 mL on each side) flowed through the felt electrodes at a flow rate of 50 mL min^{-1} by using a BT100-1L peristaltic pump (LONGER, China). Galvanostatic charge/discharge cycling curves were obtained on LAND CT2001A cell test system (LAND, CHINA). The mixed-reactant electrolyte consisting of 1:1 mixture of azoB and DBMMB in TEATFSI/MeCN is used as both anolyte and catholyte. In the solvent comparison experiment, the electrolytes with 10 mM azoB/10 mM DBMMB in 1.0 M TEATFSI/solvent (MeCN or DMF) were employed as catholyte and anolyte, respectively. The electrochemical impedance spectroscopy (EIS) test was conducted on a VersaSTAT 3 electrochemical workstation over the frequency of 10^5–1 Hz with a perturbation amplitude of 10 mV at the open circuit condition. The I-V polarization curves were measured by a series of galvanostatic discharge steps, starting from ~ 100% state of charge (SOC) [23, 24]. The current steps lasted 30s each to allow the system to stabilize. Discharge was terminated when the cell voltage dropped below 0.2 V. The average cell potential at the specified current provides a point on the polarization curve. A steady current below 2 mA cm^{-2} at a cell potential of 2.8 V was taken to indicate ~ 100% SOC.

2.3. Solubility test

The solubility of azoB in 1.0 M TEATFSI/MeCN was monitored by CV of the diluted saturated solution [6]. First, a series of standard concentration solutions are configured. 5-10 mM azoB was dissolved in 1.0 M TEATFSI/MeCN. Azobenzene was gradually added to 5 mL of 1.0 M TEATFSI/MeCN, and dissolved by ultrasonic treatment until the added material no longer dissolved, thus forming a saturated solution. The saturated solution was allowed to stand overnight, after which the supernatant was diluted with 1.0 M TEATFSI/MeCN. Finally, the CV test is performed on the diluted electrolyte. For the Nernst system, the peak current is proportional to the concentration according to the Randles-Sevcik equation. Furthermore, a calibration curve was obtained through the linear relationship between the cathodic current and the concentration of azoB. The solubility of azoB in 1.0 M TEATFSI/MeCN was extrapolated based on the calibration curve.

2.4. Other characterization

For the analysis of the changes of the electrolyte before and after cycling test, a small amount of electrolyte was taken out after a certain number of cycles, diluted and carried out the Fourier transform infrared spectroscopy (FTIR, NEXUS 670) and Ultraviolet-visible Spectrophotometer (UV-vis, Shimadzu UV-2450 spectrometer) tests in time.

3. Results and discussion

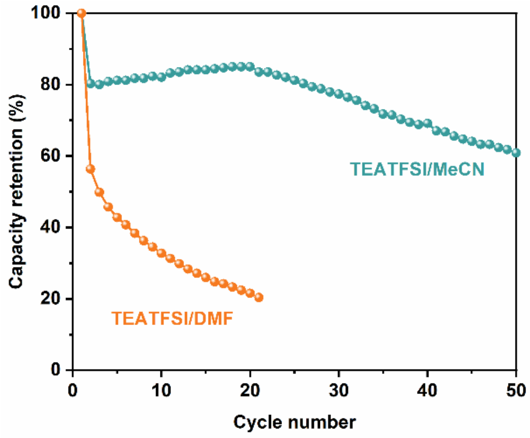

Fig. 1. Cycling capacity retention of the flow cells with different solvents at 20 mA cm^{-2}. The anolyte and catholyte are mixed-reactant electrolyte of 10 mM azoB/10 mM DBMMB in 1.0 M TEATFSI/solvent (MeCN or DMF).

The performance of NARFBs is closely related to the solvent, since it partly determines the chemical stability of active materials and the ionic conductivity of the electrolyte [5]. To find an appropriate solvent for the azoB/DBMMB active species with TEATFSI as the support electrolyte, two kinds of solvent, MeCN and DMF, were examined in the cell assembled with 10 mL of 10 mM azoB and 10 mM DBMMB in 1.0 M TEATFSI/solvent as catholyte and anolyte with Daramic-175 separator. At *j* of 20 mA cm^{-2}, the capacity decays rapidly when DMF is utilized as the solvent (Fig. 1), in agreement with the report [19]. It is probably due to the lone electron pairs of the oxygen atom of the DMF molecules, which promote the deprotonation of $DBMMB^{\bullet +}$, leading to irreversible parasitic reactions [25, 26]. In sharp contrast, the cell with MeCN solvent shows rather stable performance over 50 cycles with average discharge capacity of 0.24 Ah L^{-1}, close to the theoretical one (0.268 Ah L^{-1}). It indicates that MeCN provides a more stable electrochemical environment for the azoB/DBMMB active species. Furthermore, MeCN has lower viscosity (0.341 vs. 0.802 mPa s) than and comparable relative permittivity (35.9 vs. 36.7) with DMF, leading to higher ion conductivity, which is beneficial for the fast charge/discharge process [1, 5]. Correspondingly, the following tests were all carried out with the MeCN solvent.

CV was run to determine the OCV of NARFB. Fig. 2 displays the CV curves of 10 mM mixed redox-active materials in 50 mM TEATFSI/MeCN at a scan rate of 100 mV s^{-1}. The half wave potentials of azoB anolyte and DBMMB catholyte are -1.76 and 0.74 V vs Ag/Ag^{+}, respectively, leading to an OCV of 2.50 V for the azoB/DBMMB RFB. Such OCV value is higher than that of many NARFBs, such as 1.21 V for 9-fluorenone/5,10-bis(2-methoxyethyl)-5,10-dihydrophenazine (FL/BMEPZ) [27], 1.80 V for N-butyl-phthalimide/1,1-dimethylferrocene (BuPh/DMFc) [28], and 2.30 V for N-methylphthalimide (MePh)/DBMMB [9]. Although it is similar with that reported for the same active actives (~2.5 V), some unknown peaks appeared at -0.3 and -0.6 V vs Ag/Ag^{+} in

LiTFSI/DMF supporting electrolyte in previous work [19], which inferred some possible parasitic reactions. In contrast, the CV curves of azoB/DBMMB in TEATFSI/MeCN here exhibit only two corresponding redox couples in the full potential range.

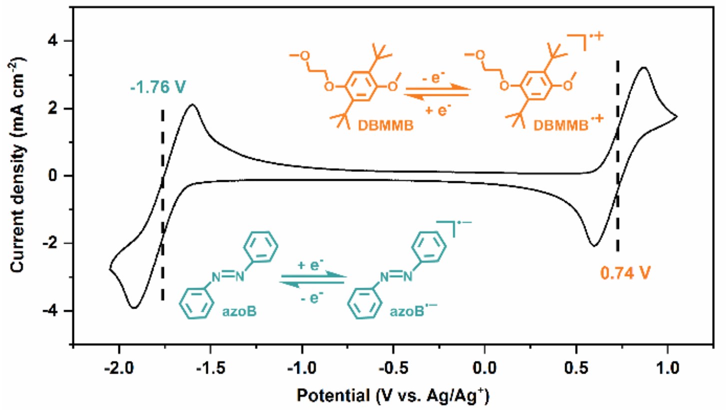

Fig. 2. CV curve of 10 mM azoB and 10 mM DBMMB in 50 mM TEATFSI/MeCN at a scan rate of 100 mV s^{-1}.

The solubility of azoB in 1 M TEATFSI/MeCN was measured by CV of the diluted saturated solution [6], which is 0.73 M. Combined with the miscibility of DBMMB, the theoretical energy density of this cell has the potential to reach 40.1 Wh L^{-1} (based on our extrapolated solubility data of 3.2 M for DBMMB), superior to most NARFBs with organometallics active materials (e.g. 11 Wh L^{-1} for Fc1N112-TFSI/Fe(acac)$_3$ [7], 18 Wh L^{-1} for V(acac)$_3$ [29], 25 Wh L^{-1} for Co(phen)$_3$/Fe(phen)$_3$ [30]), and still higher than conventional NARFBs based on ROMs (e.g. 28.6 Wh L^{-1} for DBMMB/Fl [8], and 35.4 Wh L^{-1} for DBMMB/MePh [9]).

To investigate the diffusion coefficients (D) and electron-transfer kinetics (k_0) of active materials in TEATFSI/MeCN, we carried out LSV test using RDE. Electrolytes containing 10 mM azoB or DBMMB in 1.0 M TEATFSI/MeCN were configured and tested at 100-600 rpm. The results are displayed in Fig. 3a, where well-defined plateaus correspond to mass-transport-controlled limiting currents (i_L). With reference to the Levich equation [9], linear relationships are found between i_L and the square root of rotation speeds ($\omega^{1/2}$). D is calculated to be 5.5×10^{-6} and 1.0×10^{-5} cm^2 s^{-1} for azoB and DBMMB, respectively (Fig. 3b). According to Koutecky-Levich analysis (Fig. 3c-e) [9], k_0 is estimated to be 5.0×10^{-3} cm s^{-1} for azoB reduction and 1.2×10^{-2} cm s^{-1} for DBMMB oxidation. The value for DBMMB is similar to that reported [10, 22]. Compared with the reported for azoB (D and k_0 are 7.75×10^{-6} cm^2 s^{-1} and 4.53×10^{-3}, respectively) [19], the slight difference is probably due to the differences in types and concentration of the supporting electrolytes (TEATFSI/MeCN vs LiTFSI/DMF). Such high diffusion capability and fast electron-transfer processes of the active materials are beneficial for low activation polarization loss and high EEs especially at high current densities.

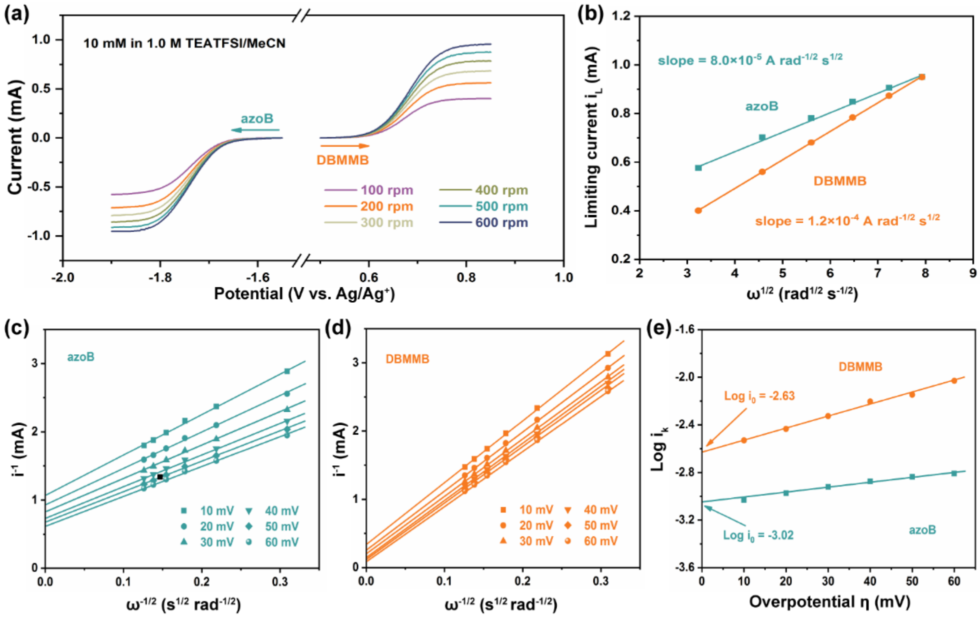

Fig. 3. (a) LSV curves of 10 mM azoB or DBMMB in 1 M TEATFSI/MeCN at a scan rate of 5 mV s^{-1}. (b) Linear Levich plots of limiting current (i_L) with respect to the square root of rotation rates ($\omega^{1/2}$). (c- e) Koutecky-Levich analysis to calculate the electron-transfer kinetics.

As aforementioned, the NARFBs usually work at low *j* (< 40 mA cm^{-2}), because higher *j* results in higher cell polarization and thus lower VE. The π-conjugated molecule of azoB is conducive to the rapid electron transfer [31, 32], matching DBMMB with high diffusion coefficient and electron-transfer kinetics [10, 22], which will mitigate the polarization loss. In addition, TEATFSI/MeCN electrolyte and Daramic 175 separator were selected for their high ion conductivity, stability, and low internal resistance. All are beneficial for high *j* operation.

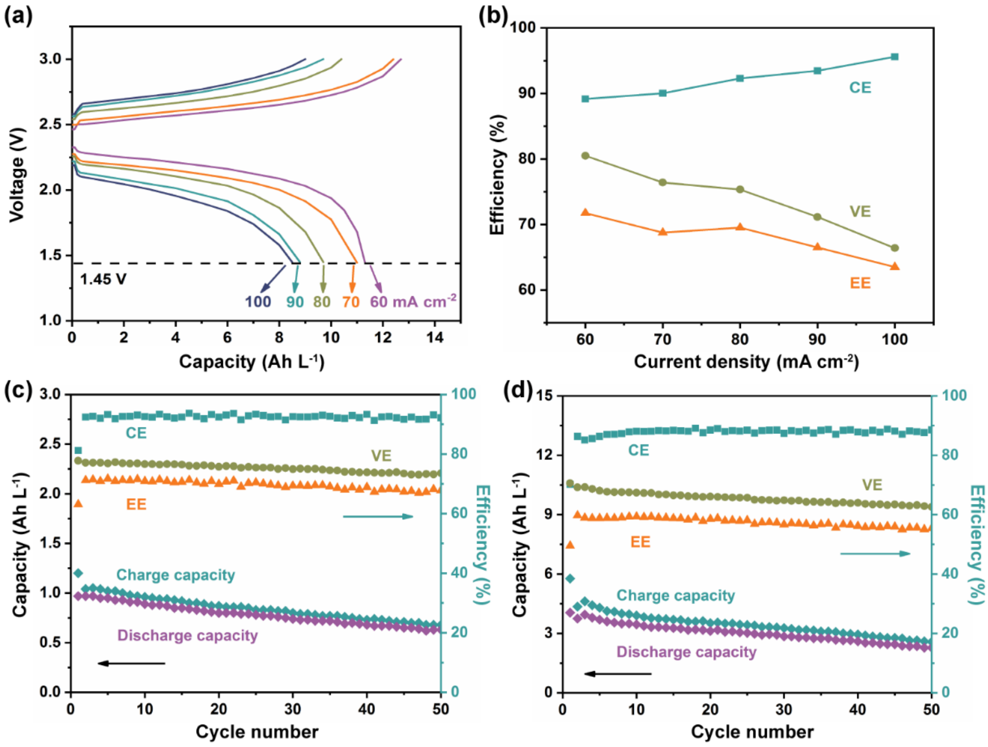

Fig. 4. (a) Typical charge/discharge profiles, (b) efficiencies at different current densities from 60 to 100 mA cm^{-2} and (c) cycling efficiency and capacity at 80 mA cm^{-2} for the battery with 0.05 M azoB/0.05 M DBMMB in 1.0 TEATFSI/MeCN. (d) Cycling efficiency and capacity for the battery with 0.25 M azoB/0.25 M DBMMB in 1.2 TEATFSI/MeCN at 100 mA cm^{-2}. The theoretical capacities are 1.34 and 6.7 Ah L^{-1} for flow cells based on 0.05 M azoB/0.05 M DBMMB and 0.25 M azoB/0.25 M DBMMB, respectively.

To prove that, the cell with mixed-reactant electrolyte of 0.05 M azoB/0.05 M DBMMB in 1.0

M TEATFSI/MeCN as catholyte and anolyte was examined for charge-discharge cycling at different *j* (60-100 mA cm^{-2}), 50 cycles at each *j*. The galvanostatic charge/discharge curves at the 2nd cycle are depicted in Fig. 4a as an example. The polarization loss of the battery increases with *j*. The discharge capacity decreases from 1.13 to 0.88 Ah L^{-1} when *j* increases from 60 to 100 mA cm^{-2}. Fig. 4b summarizes the average Coulombic efficiency (CV), VE and EE as a function of *j*. Fig. 4c is the detailed cycling profile at 80 mA cm^{-2}. When *j* increases from 60 to 100 mA cm^{-2}, the average CE increases from 89.1% to 95.6% due to weaker crossover effect. It also suggests that the crossover effect cannot be eliminated even at a mixed-reactant electrolyte. Although both VE and EE decrease due to the increased electrochemical polarization, VE and EE still remain 66.4% and 63.5% even at 100 mA cm^{-2}, indicating the robustness of the cell with the tested components [33].

To further explore the battery performance, a battery with 0.25 M azoB/0.25 M DBMMB in 1.2 M TEATFSI/MeCN was assembled and tested at 100 mA cm^{-2}. As shown in Fig. 4d, the battery can work under such a harsh condition. The average CE, VE, EE and discharge capacity are 87.5%, 65.5%, 57.4% and 3.02 Ah L^{-1}, respectively. The CE lower than 100% is due to the crossover effect [34, 35] and/or self-discharge process [36]. VE and EE also maintain at acceptable levels considering the extremely high *j* (Table 1).

Table 1 Comparison of the electrochemical performance of NARFBs.

Cathode/Anode	Electrolyte	Voltage (V)	*j* (mA cm^{-2})	CE/VE/EE (%)	Cycle number	Ref.
0.1 M DBMMB/F-FL	1.0 M TEATFSI/DME	2.37	10	95/85/81	50	[8]
0.3 M DBMMB/MePh	1.0 M LiTFSI/DME	2.3	35	90/77/69	50	[9]
0.1 M DBMMB/BzNSN	1.0 M LiTFSI/MeCN	2.36	40	95/73/69	150	[10]
0.1 M DBMMB/2-MBP	0.5 M TEAPF$_6$/MeCN	2.97	7.5	95/74/70	50	[11]
0.1 M Fc/azoB	0.5 M LiTFSI/DMF	1.78	20	99/-/-	450	[19]
0.1 M azoB/Li	0.5 M LiTFSI/DMF	1.54	0.2	88/-/-	3000	[19]
0.05 M DBMMB/azoB	1.0 M TEATFSI/MeCN	2.50	80	92/75/70	50	This work
0.25 M DBMMB/azoB	1.2 M TEATFSI/MeCN	2.50	100	88/66/58	50	

Note: F-FL: 2-fluoro-9-fluorenone; 2-MBP: 2-methylbenzophenone; Fc: ferrocene.

Fig. 5a shows the polarization curves of NARFB with 0.05 M azoB/0.05 M DBMMB and 0.25 M azoB/0.25 M DBMMB, respectively. The OCV of the cell is ~2.50 V, consistent with the CV result (Fig. 2). Ohmic polarization at low current densities and concentration polarization at high current densities are mainly responsible for the voltage losses. The azoB/DBMMB cell can achieve a peak power density of 227 mW cm^{-2} for 0.05 M azoB/0.05 M DBMMB and 336 mW cm^{-2} for 0.25 M azoB/0.25 M DBMMB. The performance rivals the acidic and alkaline aqueous flow batteries and outperforms almost all the nonaqueous flow cells (Fig. 5b) [19, 26, 37-43]. Such an unprecedented power density is related to the synergetic effect of electrolyte, separator, and active materials [1].

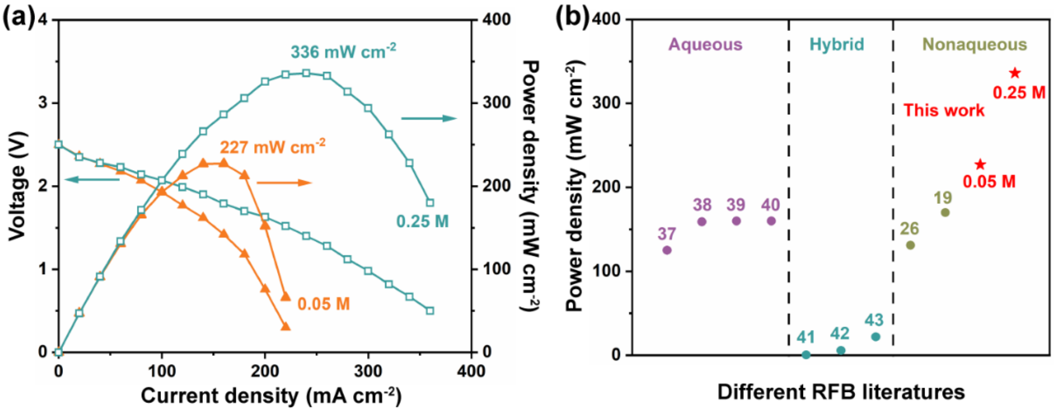

Fig. 5. (a) Current density-voltage and current density-power density profiles of NARFBs assembled with 0.05 M azoB/0.05 M DBMMB and 0.25 M azoB/0.25 M DBMMB, respectively. (b) Comparison of power density of NARFBs. The numbers labeled are references.

To further examine the stability of the active materials, FTIR and UV–vis spectra were collected intermittently and the results are shown Fig. 6a and b, respectively. The fully recovered FTIR and UV-vis curves of cycled electrolytes demonstrate the excellent reversibility of the redox-active materials. The sample after 50 charge/discharge cycles is basically the same as the original one, indicating negligible side reactions. To further examine the membrane, the membrane resistance was examined by EIS and the results are shown in Fig. 6c. The semicircle at the high frequencies is associated with the electrode and mass transfer process, and that at the low frequency may be due to a film on the electrode surface formed either by precipitation of active materials or by decomposition of the supporting electrolyte or solvent [44]. The change in EIS at low frequency region occurs from the first cycle, which is probably responsible for the lowest CE in the first cycle [44]. The intercept of the high frequency semicircle with the horizontal axis is dominated by the membrane resistance, which remains constant at ~3.5 Ω cm^2. It infers that the porous Daramic 175 separator was stable over 50 cycles. The CV curves of both anolyte and catholyte after 50 cycles (Fig. 6d) also suggest high chemical and electrochemical stability of the azoB-DBMMB active materials. Such results confirm that the irreversible degradation of redox-active materials is relatively low in this work, distinctively different from the reported [7, 22]. After cell test, orange electrolyte is observed on the membrane, gaskets and graphite plate, indicating the leakage of the electrolyte, which has been found in our previous work [22] and should be partly responsible for the capacity loss. The capacity loss may be also originated from the unbalanced redox material transport, poor ion selectivity of porous membrane [7, 22], which remains to be explored.

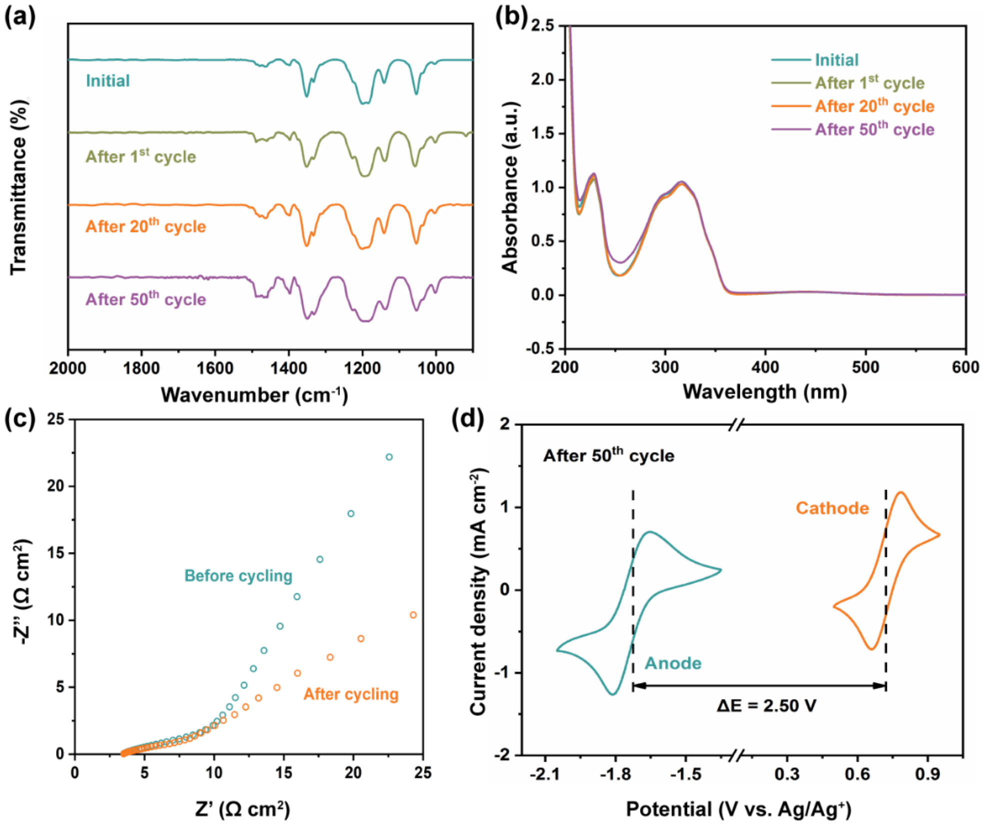

Fig. 6. (a) FTIR spectra and (b) UV-Vis absorption spectra of anode electrolyte before and after 1 cycle, 20 cycles and 50 cycles. (c) EIS of the cell before and after 50 cycles at 80 mA cm^{-2}. (d) CV curves of the anode and cathode electrolytes after 50 cycles.

4. Conclusions

The performance of NARFB with azoB and DBMMB active materials can be substantially improved by optimizing the solvent, supporting electrolyte, and membrane, especially at high current densities. The solvent plays an important role. Acetonitrile is a suitable solvent for the TEATFSI supporting electrolyte and azoB/DBMMB active materials. The battery with mixed-reactant electrolyte of 0.05 M azoB/0.05 M DBMMB in 1.0 TEATFSI/MeCN as anolyte and catholyte achieves average CE, VE and EE of 92.3%, 75.3%, 69.5%, respectively, at 80 mA cm^{-2} over 50 cycles. When j increases to 100 mA cm^{-2}, it delivers average CE, VE and EE of 87.5%, 65.5% and 57.4%, respectively, with 0.25 M azoB/0.25 M DBMMB in 1.2 M TEATFSI/MeCN. The battery delivers a peak power density of 336 mW cm^{-2} at j of 240 mA cm^{-2} with 0.25 M active materials, which is a new benchmark for NARFBs. Such outstanding performance is attributed to the synergistic effect of the high electrolyte conductivity, low resistance of the separator, fast diffusion coefficient and reaction kinetics of redox-active species and high cell voltage. The high operation current density and power density can reduce the time and capital costs, which is beneficial for future practical application.

Declaration of competing interest

The authors declare that they have no known competing financial interests or personal relationships that could have appeared to influence the work reported in this paper.

Acknowledgements

The work was financially supported by the National Natural Science Foundation of China (21636007).

References

[1] Y. Ding, C. Zhang, L. Zhang, Y. Zhou, G. Yu, Chem. Soc. Rev. 47 (2018) 69-103.

[2] P. Leung, X. Li, C.P. de Leon, L. Berlouis, C.T.J. Low, F.C. Walsh, RSC Adv. 2 (2012) 10125-10156.

[3] G. Soloveichik, Chem. Rev. 115 (2015) 11533-11558.

[4] W. Wang, Q. Luo, B. Li, X. Wei, L. Li, Z. Yang, Adv. Funct. Mater. 23 (2013) 970-986.

[5] K. Gong, Q. Fang, S. Gu, S. Li, Y. Yan, Energy Environ. Sci. 8 (2015) 3515-3530.

[6] K.H. Hendriks, S.G. Robinson, M.N. Braten, C.S. Sevov, B.A. Helms, M.S. Sigman, S.D. Minteer, M.S. Sanford, ACS Cent. Sci. 4 (2018) 189-196.

[7] Y. Zhen, C. Zhang, J. Yuan, Y. Zhao, Y. Li, J. Power Sources 445 (2020) 227331.

[8] X. Wei, W. Xu, J. Huang, L. Zhang, E. Walter, C. Lawrence, M. Vijayakumar, W.A. Henderson, T. Liu, L. Cosimbescu, B. Li, V. Sprenkle, W. Wang, Angew. Chem. Int. Ed. 54 (2015) 8684-8687.

[9] X. Wei, W. Duan, J. Huang, L. Zhang, B. Li, D. Reed, W. Xu, V. Sprenkle, W. Wang, ACS Energy Lett. 1 (2016) 705-711.

[10] W. Duan, J. Huang, J. Kowalski, I.A. Shkrob, M. Vijayakumar, E. Walter, B. Pan, Z. Yang, J.D. Milshtein, B. Li, C. Liao, Z. Zhang, W. Wang, J. Liu, J.S. Moore, F.R. Brushett, L. Zhang, X. Wei, ACS Energy Lett. 2 (2017) 1156-1161.

[11] X. Xing, Q. Liu, W. Xu, W. Liang, J. Liu, B. Wang, J.P. Lemmon, ACS Appl. Energy Mater. 2 (2019) 2364-2369.

[12] V. Viswanathan, A. Crawford, D. Stephenson, S. Kim, W. Wang, B. Li, G. Coffey, E. Thomsen, G. Graff, P. Balducci, M. Kintner-Meyer, V. Sprenkle, J. Power Sources 247 (2014) 1040-1051.

[13] H.R. Jiang, J. Sun, L. Wei, M.C. Wu, W. Shyy, T.S. Zhao, Energy Storage Mater. 24 (2020)

529-540.

[14] W. Lu, X. Li, H. Zhang, Phys. Chem. Chem. Phys. 20 (2018) 23-35.

[15] S. Hwang, H.S. Kim, J.H. Ryu, S.M. Oh, J. Power Sources 395 (2018) 60-65.

[16] Z. Li, S. Li, S. Liu, K. Huang, D. Fang, F. Wang, S. Peng, Electrochem. Solid-State Lett. 14 (2011) A171-A173.

[17] M. Milton, Q. Cheng, Y. Yang, C. Nuckolls, R.H. Sanchez, T.J. Sisto, Nano Lett. 17 (2017) 7859-7863.

[18] Y. Huo, X. Xing, C. Zhang, X. Wang, Y. Li, RSC Adv. 9 (2019) 13128-13132.

[19] L. Zhang, Y. Qian, R. Feng, Y. Ding, X. Zu, C. Zhang, X. Guo, W. Wang, G. Yu, Nat. Commun. 11 (2020) 3843.

[20] X. Wei, L. Li, Q. Luo, Z. Nie, W. Wang, B. Li, G. Xia, E. Miller, J. Chambers, Z. Yang, J. Power Sources 218 (2012) 39-45.

[21] J. Huang, L. Cheng, R.S. Assary, P. Wang, Z. Xue, A.K. Burrell, L.A. Curtiss, L. Zhang, Adv. Energy Mater. 5 (2015) 1401782.

[22] J. Yuan, C. Zhang, Y. Zhen, Y. Zhao, Y. Li, J. Power Sources 443 (2019) 227283.

[23] D. Aaron, Z.J. Tang, A.B. Papandrew, T.A. Zawodzinski, J. Appl. Electrochem. 41 (2011) 1175-1182.

[24] I. Mayrhuber, C.R. Dennison, V. Kalra, E.C. Kumbur, J. Power Sources 260 (2014) 251-258.

[25] E.A. Khatuntseva, M.A. Krest'yaninov, I.V. Fedorova, M.G. Kiselev, L.P. Safonova, Russ. J. Phys. Chem. 89 (2015) 2248-2253.

[26] R.S. Assary, L. Zhang, J. Huang, L.A. Curtiss, J. Phys. Chem. C. 120 (2016) 14531-14538.

[27] G. Kwon, K. Lee, M.H. Lee, B. Lee, S. Lee, S.K. Jung, K. Ku, J. Kim, S.Y. Park, J.E. Kwon, K. Kang, Chem 5 (2019) 2642-2656.

[28] C. Zhang, Y. Qian, Y. Ding, L. Zhang, X. Guo, Y. Zhao, G. Yu, Angew. Chem. Int. Ed. 58 (2019) 7045-7050.

[29] I.L. Escalante-Garcia, J.S. Wainright, L.T. Thompson, R.F. Savinell, J. Electrochem. Soc. 162 (2015) A363-A372.

[30] X. Xing, Y. Zhao, Y. Li, J. Power Sources 293 (2015) 778-783.

[31] C. Luo, G. Xu, X. Ji, S. Hou, L. Chen, F. Wang, J. Jiang, Z. Chen, Y. Ren, K. Amine, C. Wang, Angew. Chem. Int. Ed. 57 (2018) 2879-2883.

[32] C. Wang, Y. Xu, Y. Fang, M. Zhou, L. Liang, S. Singh, H. Zhao, A. Schober, Y. Lei, J. Am. Chem. Soc. 137 (2015) 3124-3130.

[33] Z. Li, Y. Lu, Adv. Mater. (2020) A171-A173.

[34] S.E. Doris, A.L. Ward, A. Baskin, P.D. Frischmann, N. Gavvalapalli, E. Chenard, C.S. Sevov, D. Prendergast, J.S. Moore, B.A. Helms, Angew. Chem. Int. Ed. 56 (2017) 1595-1599.

[35] G. Li, Y. Jia, S. Zhang, X. Li, J. Li, L. Li, J. Appl. Electrochem. 47 (2017) 261-272.

[36] A. Tang, J. Bao, M. Skyllas-Kazacos, J. Power Sources 216 (2012) 489-501.

[37] K. Gong, F. Xu, J.B. Grunewald, X. Ma, Y. Zhao, S. Gu, Y. Yan, ACS Energy Lett. 1 (2016) 89-93.

[38] B. Hu, C. DeBruler, Z. Rhodes, T.L. Liu, J. Am. Chem. Soc. 139 (2017) 1207-1214.

[39] Q. Huang, J. Yang, C.B. Ng, C. Jia, Q. Wang, Energy Environ. Sci. 9 (2016) 917-921.

[40] J. Luo, B. Hu, C. Debruler, Y. Bi, Y. Zhao, B. Yuan, M. Hu, W. Wu, T. Liu, Joule 3 (2019)

149-163.

[41] A. Orita, M.G. Verde, M. Sakai, Y.S. Meng, Nat. Commun. 7 (2016) 13230.

[42] L. Zhang, C. Zhang, Y. Ding, K. Ramirez-Meyers, G. Yu, Joule 1 (2017) 623-633.

[43] Y. Zhu, T.M. Narayanan, M. Tulodziecki, H. Sanchez-Casalongue, Q.C. Horn, L. Meda, Y. Yu, J. Sun, T. Regier, G.H. McKinley, Y. Shao-Horn, Sustain. Energy Fuels 4 (2020) 4076-4085.

[44] I. L. Escalante-Garcia, J. S. Wainright, L. T. Thompson, R. F. Savinella, J. Electrochem. Soc. 162 (2015) A363-A372.